PHYSICS OF FLUIDS **25**, 033602 (2013)

Inertial particle trapping in viscous streaming

Kwitae Chong,[1] Scott D. Kelly,[2] Stuart Smith,[2] and Jeff D. Eldredge[1,a)]
[1]*Mechanical and Aerospace Engineering, University of California, Los Angeles, Los Angeles, California 90095, USA*
[2]*Mechanical Engineering and Engineering Science, The University of North Carolina at Charlotte, Charlotte, North Carolina 28223, USA*

(Received 21 November 2012; accepted 7 March 2013; published online 28 March 2013)

The motion of an inertial particle in a viscous streaming flow of Reynolds number order 10 is investigated theoretically and numerically. The streaming flow created by a circular cylinder undergoing rectilinear oscillation with small amplitude is obtained by asymptotic expansion from previous work, and the resulting velocity field is used to integrate the Maxey–Riley equation with the Saffman lift for the motion of an inertial spherical particle immersed in this flow. It is found that inertial particles spiral inward and become trapped inside one of the four streaming cells established by the cylinder oscillation, regardless of the particle size, density and flow Reynolds number. It is shown that the Faxén correction terms divert the particles from the fluid particle trajectories, and once diverted, the Saffman lift force is most responsible for effecting the inward motion and trapping. The speed of this trapping increases with increasing particle size, decreasing particle density, and increasing oscillation Reynolds number. The effects of Reynolds number on the streaming cell topology and the boundaries of particle attraction are also explored. It is found that particles initially outside the streaming cell are repelled by the flow rather than trapped. © *2013 American Institute of Physics*. [http://dx.doi.org/10.1063/1.4795857]

I. INTRODUCTION

Techniques for separating, focusing, and transporting small-sized particles in an aqueous environment have matured in recent years, motivated primarily by technology needs such as drug delivery, cell processing, and microfluidic devices. Some of the most notable and effective methods are based on lasers,[1–3] ultrasonics,[4,5] dielectrophoresis,[6,7] and inertial hydrodynamic effects.[8,9] Another appealing option for particle manipulation is based on the notion of steady streaming. A streaming flow is a relatively weak but large-scale steady response of a fluid to non-linear interactions – the Reynolds stresses – in a primary oscillatory flow. Such a flow can arise in both viscous and acoustic environments. The promise of such a flow for trapping and manipulating microparticles has recently been demonstrated by a number of recent studies. Lutz *et al.*[10,11] created streaming eddies around a cylinder fixed in a microchannel through which fluid was oscillated, and showed that particles both lighter and heavier than the surrounding fluid could be trapped; Lieu *et al.*[12] recently characterized the trapping in the vicinity of other obstacles, and a cavity, as well. These studies also showed that trapping was less effective when the particle was much much smaller than the cylinder.

Marmottant and Hilgenfeldt[13] exhibited controlled vesicle deformation and lysis using a single oscillating microbubble mounted on the wall of a microchannel. The shear force on the vesicles due to the streaming flow was strong enough to deform and rupture them. They also demonstrated microparticle transport based on a controlled fluid motion created through combinations of oscillating bubbles.[14,15] Wang *et al.*[16] have recently demonstrated the size-selective trapping and release of microparticles through a superposition of bubble-induced streaming and Poiseuille flow.

[a)] Author to whom correspondence should be addressed. Electronic mail: eldredge@seas.ucla.edu

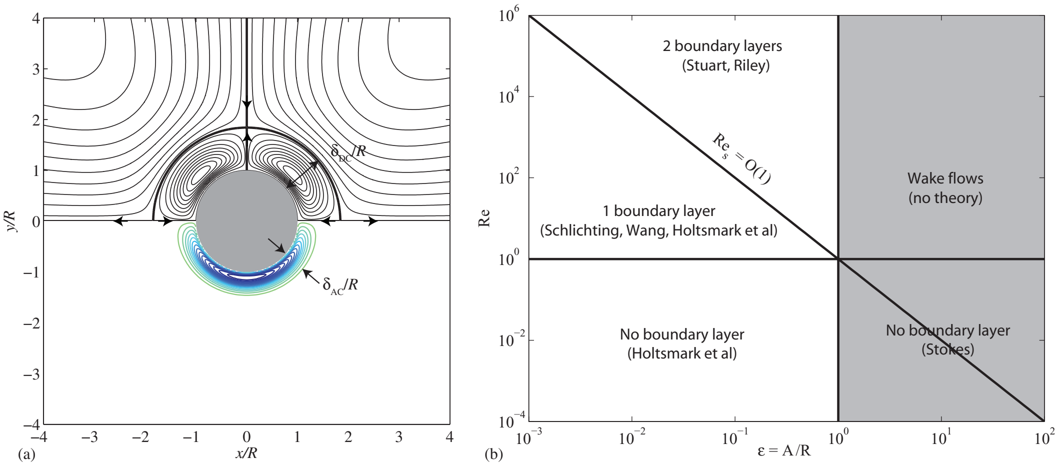

FIG. 1. (a) Lagrangian streamlines (top half) and instantaneous Stokes-layer vorticity (bottom half) of canonical streaming pattern for $Re \gg 1$ and $Re_s \ll 1$ (here, $Re = 80$). (b) Streaming regimes (adapted from Wang[20]).

These recent works demonstrate the excellent opportunities for particle manipulation using streaming flows. In this work, we are interested in obtaining a deeper understanding of the behavior of a canonical streaming flow (the flow generated by an oscillating circular cylinder), and particularly, the interaction of small inertial particles with such a flow. Though it is known that particles can be trapped by the streaming, relatively little is known about the nature or conditions under which this trapping is possible. Here, our objective is to provide more physical intuition and to determine the dependence on various parameters, such as Reynolds number, and particle size, and relative density.

The study of steady streaming dates to Lord Rayleigh, who found the existence of a steady flow in Kundt's tube.[17] Early experimental studies of viscous streaming in the vicinity of a circular cylinder (and other obstacles) were conducted by Andrade[18] who mounted the cylinder in an apparatus through which air was driven sinusoidally. Smoke was used to visualize the cloverleaf pattern of streaming cells. Schlichting[19] examined the same flow, generated in this case by an oscillating cylinder in an otherwise quiescent medium. His study was notable for providing a theoretical analysis of the flow, based on an expansion in the ratio ϵ of small oscillation amplitude A to cylinder radius R. The analysis was performed in a reference frame attached to the oscillating body, so that the fluid at infinity is in uniform oscillation. Schlichting matched the inner flow solution – in which the relevant length scale is the thickness of the oscillatory (Stokes) boundary layer, $\delta_{AC} = (\nu/\Omega)^{1/2}$, where ν is kinematic viscosity and Ω is angular frequency of oscillation – with a corresponding expansion of the outer flow. The leading-order outer potential flow drives the Stokes layer near the cylinder, which applies a second-order correction to the outer flow due to displacement, which in turn affects the boundary layer at the next order, and so on. It is useful to note that the thickness of the Stokes layer is directly related to the Reynolds number based on cylinder radius: $\delta_{AC}/R = 1/Re^{1/2}$, where $Re = \Omega R^2/\nu$.

The steady component of the flow enters at second order, driven by the mean Reynolds stress of the leading-order Stokes layer. This steady flow is divided into four equal quadrants about the cylinder by the axis of oscillation and the axis transverse to this oscillation (see Figure 1(a), which also depicts the vorticity in the Stokes layer). Each quadrant exhibits a streaming cell, segregated from the outer flow by a dividing streamline at distance δ_{DC} off the surface of the cylinder. The Reynolds stresses decay exponentially with distance from the cylinder surface, so the fluid outside the boundary layer is set in steady motion indirectly, effectively dragged along by the inner flow. The composite of these inner and outer flows represents the streaming flow.

Schlichting's analysis provided an intuitive understanding of the flow that subsequent analyses have improved upon, but not significantly altered. Wang[20] argued that body curvature, which Schlichting neglected, should have an important influence on the boundary layer behavior; however, this influence is only felt at second order and higher in the oscillatory portion, and third order and higher in the steady portions of the flow, as revealed by Wang's matched asymptotic analysis. Holtsmark *et al.*[21] also performed an asymptotic expansion in small amplitude ratio, but did not treat the inner and outer flows separately; rather, they solved for the entire flow about the cylinder at each order of accuracy. The results of Holtsmark *et al.*[21] contain those of Schlichting[19] and Wang[20] when one carries out an expansion of these results in powers of $Re^{-1/2}$, assuming that $Re \gg 1$; however, the Holtsmark group's result holds equally well for moderate and small Re, for which the oscillatory boundary layer is absent. Raney, Corelli, and Westervelt[22] and later Bertelsen, Svardal, and Tjøtta[23] corrected each of these results for the Stokes drift, which accounts for the difference between the steady Lagrangian streamlines (the mean paths followed by fluid particles) and the Eulerian streamlines (which are obtained from the mean streamfunction). Since most experimental measurements of the flow are based on tracking the motion of passive tracer particles, the Stokes drift is inherent to such experimental results. As is apparent from the experiments from Holtsmark *et al.*[21] and corroborated by the drift-corrected theory,[23] the relative thickness, δ_{DC}/R, of the inner streaming cell exhibits a complex dependence on the Reynolds number, growing progressively larger as Re gets smaller and without bound as $Re \to 37$ (exhibited in Figure 4). Note that $\delta_{DC}/\delta_{AC} > 1$ at all Reynolds numbers, as Figure 1(a) indicates at the particular case of $Re = 80$.

Though the Reynolds number, Re, defines the size of the driving mechanism (the Stokes layer), the streaming flow itself is characterized by a streaming Reynolds number, $Re_s = \Omega A^2/\nu$. Its role is clear from the fact that the characteristic velocity of the streaming flow is $V_s = \epsilon\Omega A$, so $Re_s = V_s R/\nu$. Each of the analyses above was based on the assumption that $Re_s \ll 1$, whereupon the steady streaming flow beyond the inner layer is essentially Stokes flow (through second order). However, when $Re_s \gg 1$, this outer flow exhibits its own boundary layer structure, with a characteristic thickness of order $R/Re_s^{1/2}$. Since $\delta_{AC} = R/Re^{1/2}$ and $Re_s = \epsilon^2 Re$, then this second boundary layer is much thicker than the Stokes layer (and the inner streaming cell, δ_{DC}). Both Riley[24] and Stuart[25] revealed the existence of such a double boundary layer structure at large streaming Reynolds number. Both authors used series expansions to arrive at this structure: Riley used the method of matched asymptotic expansions, whereas Stuart relied on a more intuitive approach.

The various streaming regimes in the ϵ–Re parametric space were nicely summarized in a figure by Wang,[20] which is presented in somewhat modified form here in Figure 1(b). The streaming theories all fall to the left of $\epsilon = O(1)$, as the right side of this line involves large-amplitude motions, which, for $Re \gg 1$ generate wake flows that resist analytical description, and for $Re \lesssim 1$ are governed by quasi-steady Stokes flow. The regime of small streaming Reynolds number lies below the line that diagonally transects the figure.

In this work, we are primarily focused on the behavior of inertial particles (particles of finite size whose density may differ from that of the surrounding fluid) in streaming flows for which $Re_s \lesssim 1$, $\epsilon \ll 1$, and $Re = O(10)$ – that is, the cases for which the theoretical treatment of Holtsmark *et al.*[21] is valid. We will assume that the particle is a rigid sphere, and sufficiently small such that its "slip" Reynolds number, $Re_p = a|\boldsymbol{w}|/\nu$ (the Reynolds number based on the velocity of the particle relative to the local undisturbed flow, $\boldsymbol{w}$, and particle radius, a) and shear Reynolds number, $Re_G = a^2 G/\nu$ (the Reynolds number based on the velocity gradient, G) are both much less than unity. The translation of a rigid sphere in this regime was originally treated separately by Basset,[26] Boussinesq,[27] and Oseen[28] (and hence the equation governing its dynamics is sometimes called the "BBO" equation). Later, Maxey and Riley[29] proposed a corrected equation of motion for a small rigid sphere in a nonuniform flow. We will make use of the equation derived in this latter work, including the Saffman lift force term[30] (and refer to it from hereon as the Maxey–Riley, or simply "MR" equation) in order to calculate trajectories of inertial particles in the flows predicted by the Holtsmark solution.

The problem statement of this study, as well as the methodology, will be described in Sec. II. In the Appendix, we summarize the Holtsmark solution, along with the correction for Stokes drift and for the change of reference frame to an oscillating circular cylinder in a quiescent flow. (This frame, in contrast to the one in which the cylinder is fixed in an oscillating flow, will enable opportunities for studying particle transport between multiple oscillators of possibly different frequencies in future work.) The Maxey–Riley equation and our technique for integrating it is also described in Sec. II. The motion of an inertial particle will be examined in Sec. III. The transient behavior of the inertial particle in the streaming cell, the dominant forces acting on the particle, and the trapping speed and equilibrium trajectory will be examined in this section. Then, concluding remarks will follow in Sec. IV.

II. PROBLEM STATEMENT AND METHODOLOGY

In this work, we study the motion of inertial particles in a flow generated by a two-dimensional circular cylinder of radius R that undergoes rectilinear sinusoidal oscillations along the x axis with amplitude A and angular frequency Ω,

$$\boldsymbol{X}(t) = e_x A \sin \Omega t \tag{1}$$

in a quiescent incompressible medium of uniform density ρ_f and kinematic viscosity ν. The y axis represents the transverse direction in the plane of the cylinder cross-section, and the z axis is parallel to the cylinder axis. A particle has radius a and density ρ_p, where it is assumed that a is much smaller than the radius of the oscillating cylinder.

It is important to consider the wide range of time scales of this problem. Inertial particles are transported approximately at the characteristic (drift-corrected) speed of the streaming flow, $V_s = \epsilon \Omega A$, around a cell of characteristic size δ_{DC}. Though this size varies with Reynolds number, as described above, it remains $O(R)$ over a wide range of Re. Thus, the convective time for a particle to orbit the streaming cell is of order $\delta_{DC}/V_s \sim R/(\epsilon \Omega A) = 1/(\epsilon^2 \Omega)$, or ϵ^{-2} periods of oscillation, and to discern long-term behavior of the particle, many such orbits must be captured. So in practice, particle trajectories must be computed over hundreds to thousands of oscillation cycles.

The solution for the flow generated about a circular cylinder in an oscillatory free stream is derived in the Appendix, and follows the derivation presented by Holtsmark *et al.*[21] However, this earlier work contains errors in the second-order oscillatory part of the solution, and we correct these errors here. We also include a derivation of the Stokes drift of fluid particles in this flow. In Sec. II A, we discuss how this solution is modified when the reference frame is changed to one in which the cylinder is in motion and the fluid at rest at infinity.

A. A note on the change of reference frame

Ultimately, we seek the flowfield in a reference frame in which the cylinder is in oscillatory motion and the fluid is at rest at infinity, which we term the "inertial" reference frame in this paper. It is important to note that a fixed position in this frame appears to be in motion in the cylinder-fixed reference frame used to obtain the solution of Holtsmark *et al.*[21] However, it is more natural to evaluate the solution at a fixed position in this latter frame. We need to account for this discrepancy, and as we will see, this leads to both a first- and second-order correction when reconciling the two frames. It is important that we carry out this analysis, because the motion of a particle with different density from the surrounding fluid will, in general, undergo a slightly different motion relative to the cylinder in the two different scenarios.

Let us denote the position of a fixed point in the inertial reference frame by $\boldsymbol{x} = (x, y)$ and the same point mapped to the cylinder-fixed reference frame by $\boldsymbol{\xi}(t) = (\xi(t), \eta(t))$. They are simply related by

$$\boldsymbol{\xi}(t) = \boldsymbol{x} - \boldsymbol{X}(t), \tag{2}$$

where here, in dimensionless form, $\boldsymbol{X}(t) = e_x \epsilon \sin t$. It is straightforward to show that, in a non-inertial frame in purely translational motion, the Navier–Stokes equations are unmodified (except for an addition to the pressure field).[31] The streamfunction, when evaluated at $\boldsymbol{\xi}(t)$, is related to its counterpart in the inertial reference frame (denoted by $\tilde{\psi}$) by

$$\psi(\boldsymbol{\xi}(t), t) = \tilde{\psi}(\boldsymbol{x}, t) - \left(\frac{\mathrm{d}}{\mathrm{d}t} \boldsymbol{X}(t) \times \boldsymbol{x} \right) \cdot e_z = \tilde{\psi}(\boldsymbol{x}, t) - \epsilon y \cos t. \tag{3}$$

Equation (3) can be used directly to transform the solution of Holtsmark *et al.*[21] to the inertial reference frame. However, it is enlightening to consider the effect of this change of frame in the context of the asymptotic expansion. Because the oscillations are assumed to be small, the streamfunction in the cylinder-fixed frame – when evaluated sufficiently far from the cylinder so that the modulated point remains outside the perimeter – can be expanded about the mean position, $\overline{\boldsymbol{\xi}}$, of the moving evaluation point,

$$\psi(\boldsymbol{\xi}(t), t) = \psi(\overline{\boldsymbol{\xi}}, t) + (\boldsymbol{\xi}(t) - \overline{\boldsymbol{\xi}}) \cdot \nabla\psi(\overline{\boldsymbol{\xi}}, t)) + O(|\boldsymbol{\xi}(t) - \overline{\boldsymbol{\xi}}|^2). \tag{4}$$

However, by (2), $\overline{\boldsymbol{\xi}} = \boldsymbol{x}$. That is, the mean location of the mapped point in the cylinder-fixed frame has the same nominal coordinates as the point in the inertial frame. Thus, we simply have

$$\psi(\boldsymbol{\xi}(t), t) = \psi(\boldsymbol{x}, t) - \epsilon \sin t \frac{\partial}{\partial x}\psi(\boldsymbol{x}, t) + O(\epsilon^3). \tag{5}$$

(The leading order of the omitted terms reflects that these terms are linearly related to ψ, which itself has leading order ϵ.) Thus, the relationship between streamfunction in the two frames – evaluated at the same nominal (fixed) location in each frame – can be written as

$$\tilde{\psi}(\boldsymbol{x}, t) = \psi(\boldsymbol{x}, t) + \epsilon y \cos t - \epsilon \sin t \frac{\partial}{\partial x}\psi(\boldsymbol{x}, t) + O(\epsilon^3). \tag{6}$$

Introducing the asymptotic expansion for ψ,

$$\tilde{\psi}(\boldsymbol{x}, t) = \epsilon\,(\psi_1(\boldsymbol{x}, t) + y \cos t) + \epsilon^2 \left(\psi_2(\boldsymbol{x}, t) - \sin t \frac{\partial}{\partial x}\psi_1(\boldsymbol{x}, t)\right) + O(\epsilon^3). \tag{7}$$

Thus, in order to compute the streamfunction in the inertial frame, the first-order streamfunction obtained by Holtsmark *et al.*[21] is modified by a term removing the velocity at infinity, and the second-order streamfunction is effectively corrected by the leading-order effect of the modulated field sampled by the moving evaluation point. The velocity field derived from this streamfunction consists of similar corrections.

B. Calculation of inertial particle trajectories

We are primarily interested in this work in computing the trajectory, $\boldsymbol{X}_p(t)$, of an inertial particle. These trajectories will be computed by integrating the Maxey–Riley (MR) equation with Saffman lift force,[29,32] which is based on the assumption of a rigid spherical particle with small slip Reynolds number, Re_p. We are therefore implicitly assuming that the motion of the particle does not significantly affect the flow generated by the oscillating cylinder. Use of the Saffman lift force is restricted by the condition of small slip Reynolds number ($Re_p \ll 1$) and shear Reynolds number ($Re_G \ll 1$), as well as $Re_p \ll Re_G^{1/2}$. That these conditions are satisfied in the present simulations can be demonstrated by examining a typical particle traversing the Stokes layer, where it experiences the largest slip velocity and shear. For the typical case of this study, particle size, Reynolds number and oscillation amplitude are $a/R = 0.175$, $Re = 40$, and $\epsilon = 0.2$, respectively. At time $t/T = 325.5$, when it is closest to the cylinder, $|\boldsymbol{w}| = 0.0268$ and $G = 0.695$ and thus $Re_p = 0.184 \ll 1$, $Re_G = 0.836 < 1$ and $Re_p \ll Re_G^{1/2}$. The Faxén correction terms cannot be ignored in our study, as their contribution is notable in the regions of significant vorticity, where the particle remains for most of its trajectory. We ignore the gravity terms, and are therefore left with

$$\frac{\mathrm{d}\boldsymbol{X}_p}{\mathrm{d}t} = \boldsymbol{V}_p, \tag{8}$$

$$m_p \frac{\mathrm{d}\boldsymbol{V}_p}{\mathrm{d}t} = -6\pi\rho_f \nu a \left[\boldsymbol{V}_p(t) - \boldsymbol{u}(\boldsymbol{X}_p(t), t) - \frac{1}{6}a^2\nabla^2\boldsymbol{u}(\boldsymbol{X}_p(t), t)\right] + m_f \left.\frac{D\boldsymbol{u}}{Dt}\right|_{\boldsymbol{X}_p(t)}$$
$$- \frac{1}{2}m_f \left(\frac{\mathrm{d}\boldsymbol{V}_p}{\mathrm{d}t} - \left.\frac{D\boldsymbol{u}}{Dt}\right|_{\boldsymbol{X}_p(t)} - \frac{\mathrm{d}}{\mathrm{d}t}\left[\frac{1}{10}a^2\nabla^2\boldsymbol{u}(\boldsymbol{X}_p(t), t)\right]\right)$$

$$
\begin{aligned}
&- 6\pi^{1/2}\nu^{1/2}a^2\rho_f \int_{-\infty}^{t} \frac{\mathrm{d}/\mathrm{d}\tau\left[\boldsymbol{V}_p(\tau) - \boldsymbol{u}(\boldsymbol{X}_p(\tau),\tau) - \frac{1}{6}a^2\nabla^2\boldsymbol{u}(\boldsymbol{X}_p(\tau),\tau)\right]}{\sqrt{t-\tau}}\,\mathrm{d}\tau \\
&+ 4K\rho_f a^2\left(\nu\left|G\right|\right)^{1/2}\mathrm{sgn}(G)\left|\boldsymbol{u}-\boldsymbol{V}_p\right|\boldsymbol{n}, \qquad (9)
\end{aligned}
$$

where

$$
\begin{aligned}
G = \left|\boldsymbol{u}-\boldsymbol{V}_p\right|^{-2}\Bigg[&\left(u_x - V_{p,x}\right)^2\frac{\partial u_x}{\partial y} - \left(u_y - V_{p,y}\right)^2\frac{\partial u_y}{\partial x} \\
&- \left(u_x - V_{p,x}\right)\left(u_y - V_{p,y}\right)\left(\frac{\partial u_x}{\partial x} - \frac{\partial u_y}{\partial y}\right)\Bigg] \qquad (10)
\end{aligned}
$$

and

$$\boldsymbol{n} = \left|\boldsymbol{u}-\boldsymbol{V}_p\right|^{-1}\left[-\left(u_y - V_{p,y}\right)\boldsymbol{e}_x + \left(u_x - V_{p,x}\right)\boldsymbol{e}_y\right]. \qquad (11)$$

The symbols m_p and m_f denote, respectively, the mass of the inertial particle and the displaced fluid. The vectors $\boldsymbol{V}_p$ and $\boldsymbol{u}$ are, respectively, the velocity of the inertial particle and the fluid velocity. The Saffman constant, K, is 1.615. It should be noted that G represents the coordinate-independent shear rate – the $\boldsymbol{n}$-directed gradient of the component of fluid velocity in the direction of relative particle motion – as used by Tio *et al.*[32] The operators d/dt and D/Dt denote the time derivatives along their respective sets of characteristics,

$$\frac{\mathrm{d}\boldsymbol{u}}{\mathrm{d}t} = \frac{\partial\boldsymbol{u}}{\partial t} + \boldsymbol{V}_p\cdot\nabla\boldsymbol{u}, \qquad \frac{D\boldsymbol{u}}{Dt} = \frac{\partial\boldsymbol{u}}{\partial t} + \boldsymbol{u}\cdot\nabla\boldsymbol{u}. \qquad (12)$$

The terms on the right hand side of (9) represent, respectively, the viscous Stokes drag, the fluid acceleration force, the added mass, the Basset history force, and the Saffman lift force. The terms involving the Laplacian of the fluid velocity are the Faxén corrections, which represent the effect of non-uniform fluid velocity incident upon the inertial particle.

The Basset history force (sometimes described as the "memory term") represents the cumulative influence of the diffusion of vorticity from the particle during its total traveling history. The computation of this term is extremely time consuming and memory intensive, and many studies neglect it for simplicity. However, it may lead to a physically incorrect result to omit the history term for a non-neutrally buoyant particle. Studies by Daitche and Tél,[33] Candelier, Angilella, and Souhar[34,35] and Mordant and Pintona[36] have shown that the history term can have a significant effect on the motion of an inertial particle and cannot generally be neglected. An efficient technique for computing the history force term was recently proposed by van Hinsberg, ten Thije Boonkkamp, and Clercx.[37] The integration interval is divided into two sub-intervals. The sub-interval involving more recent history is computed by trapezoidal integration; in the more distant sub-interval, the Basset kernel $t^{-1/2}$ is replaced with an exponential approximant, and a recursive algorithm is constructed to minimize expense. We adopt this approach in the present work.

Since the MR equation (9) evaluates the terms at the center of the inertial particle, it makes sense to define the relative velocity, $\boldsymbol{w} = \boldsymbol{V}_p - \boldsymbol{u}(\boldsymbol{X}_p)$, so that the relationship between time derivatives is simply

$$\frac{D\boldsymbol{u}}{Dt} = \frac{\mathrm{d}\boldsymbol{u}}{\mathrm{d}t} - \boldsymbol{w}\cdot\nabla\boldsymbol{u}. \qquad (13)$$

Furthermore, we can non-dimensionalize the variables using Ω and R, as for the flowfield itself in the Appendix. Thus, the dimensionless version of the MR equation (9) can be written as

$$
\begin{aligned}
\left(\frac{\rho_p}{\rho_f} + \frac{1}{2}\right)\frac{\mathrm{d}\boldsymbol{w}}{\mathrm{d}t} = &-\frac{9}{2}Re_a^{-1}\boldsymbol{w} + (1-\rho_p/\rho_f)\left.\frac{\mathrm{d}\boldsymbol{u}}{\mathrm{d}t}\right|_{X_p(t)} - \frac{3}{2}\boldsymbol{w}\cdot\nabla\boldsymbol{u}\Big|_{X_p(t)} \\
&-\frac{9}{2}\pi^{-1/2}Re_a^{-1/2}\int_{-\infty}^{t}\frac{\mathrm{d}/\mathrm{d}\tau\left[\boldsymbol{w} - \frac{1}{6}(a/R)^2\nabla^2\boldsymbol{u}(\boldsymbol{X}_p(\tau),\tau)\right]}{\sqrt{t-\tau}}\,\mathrm{d}\tau
\end{aligned}
$$

$$+3K Re_a^{-1/2} |G|^{1/2} \operatorname{sgn}(G)|\boldsymbol{w}|\boldsymbol{n}$$
$$+\frac{3}{4} Re_a^{-1}(a/R)^2 \nabla^2 \boldsymbol{u}(\boldsymbol{X}_p(t), t) + \frac{1}{20}(a/R)^2 \frac{\mathrm{d}}{\mathrm{d}t}\left[\nabla^2 \boldsymbol{u}(\boldsymbol{X}_p(t), t)\right], \qquad (14)$$

where $Re_a = \Omega a^2/\nu = Re(a/R)^2$ is a particle-based Reynolds number. In terms of the direction, $\hat{\boldsymbol{w}} = \boldsymbol{w}/|\boldsymbol{w}|$, of the relative velocity, the direction of Saffman lift is

$$\boldsymbol{n} = \hat{\boldsymbol{w}} \times e_z \qquad (15)$$

and the generalized shear rate is represented compactly as

$$G = \boldsymbol{n} \cdot \nabla \boldsymbol{u} \cdot \hat{\boldsymbol{w}}. \qquad (16)$$

The inertial particle initially has the same velocity as the surrounding fluid, so that the initial condition of this integro-differential equation is $\boldsymbol{w}(0) = 0$. The Stokes drag and the Basset history act as penalty terms, tending to drive $\boldsymbol{w}$ to zero when the particle's velocity deviates from that of the fluid; these terms, along with the Saffman lift, are only active when $\boldsymbol{w}$ is non-zero. The unsteady term (the second term on the right-hand side) and Faxén corrections are the only inhomogeneous terms in this equation, and we note that the first of these is absent for neutrally buoyant particles. The third term on the right-hand side, due to the differences in the advection between a fluid and inertial particle, is only significant when the particle traverses regions of steep change in fluid velocity. The equation is integrated with a 4th-order Adams-Bashforth method with time step size 0.02. At each time step, the fluid velocity, its gradient, and its time derivative are computed from the Holtsmark solution (with a correction for change of reference frame, described above) at the instantaneous location of the particle. Convergence of the time marching was tested by doubling and halving the step size, and verifying that the results were insensitive.

The relevant dimensionless parameters of this problem, in addition to the oscillatory Reynolds number Re and amplitude ratio ϵ, are the density ratio ρ_p/ρ_f and particle size ratio a/R. In this work, we will keep ϵ fixed at 0.2; this is a compromise between a sufficiently small amplitude for the asymptotic solution to hold and practical integration times for computing particle trajectories.

Finally, we note that we do not add an additional force to account for the hydrodynamic influence of the rigid cylinder on the particle. That is, the effect of the cylinder on the particle's motion is felt solely through the velocity field generated by the oscillating cylinder.

III. RESULTS

The trajectory, $\boldsymbol{X}_p(t)$, of an inertial particle is computed by integrating equation (14) for the inertial particle velocity, $\boldsymbol{V}_p$, based on the parameters of relative particle density ρ_p/ρ_f, relative size a/R and Reynolds number Re. Figure 2 depicts a visual comparison of the continuous inertial particle trajectory and the trajectory sampled once per oscillation cycle, in this case for a neutrally buoyant particle. The particle oscillates at the forcing frequency with an amplitude of approximately $0.03R$. As expected due to the small streaming velocity of order ϵ^2, the overall migration speed is very slow.

Figure 3 depicts representative trajectories for a heavy, a neutrally buoyant, and a light particle at $Re = 40$ for a particle of radius $a = 0.175R$. Each trajectory is sampled only once per cycle for clarity purposes, and thus is actually a set of discrete points representing the Poincaré section of the particle motion. Open blue circles denote the initial location, in this case at $(x, y) = (2R, 2R)$, and the mean Lagrangian streamlines are depicted for reference. Note that, at this Reynolds number, the inner streaming cell has size $\delta_{DC} \approx 4.6R$.

The plots in Figure 3 indicate that particles undergo an inward spiral toward the center of the streaming cell, regardless of their density relative to the fluid. Figure 3(d) shows that the trajectories of an inertial particle and fluid particle starting from the same initial location deviate over one oscillation cycle, with the inertial particle ultimately closer to the center of the streaming cell at the end of the cycle. The hydrodynamic force vectors shown here are computed from the right-hand side of (14), and thus are proportional to the rate of change of the relative velocity between the inertial and fluid particles. They are generally directed away from the cylinder, consistent with the deviation of the trajectories.

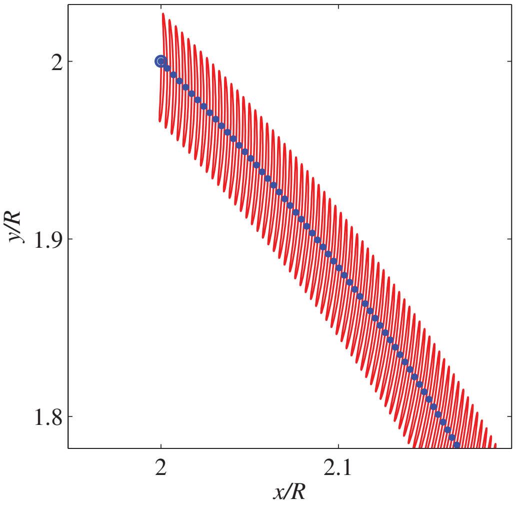

FIG. 2. Inertial particle trajectory (solid line) and trajectory sampled once per cycle (shown as dots) for $Re = 40$, $a/R = 0.175$, and $\rho_p/\rho_f = 1$.

This spiral trajectory is qualitatively similar to the trajectory of a microsphere in a micro-channel reported in the experiments of Lutz *et al.*[11] Figure 4 depicts a comparison of the final trapping position predicted in the present study with the experimental results of Lutz *et al.*,[11] at different Reynolds numbers. The size δ_{DC}/R of the inner streaming cell is also shown, and exhibits the dependence on Reynolds number reported above, increasing without bound as $Re \to 37$. The position of trapping predicted by the model agrees well with the experiments.

In order to determine whether the motion of an inertial particle shows a tendency to spiral inward or outward, it is helpful to consider the instantaneous cross product of the local tangents to the mean inertial and fluid particle trajectories, which we denote as α. If we assume that at some recent instant the inertial particle moved at the same velocity as the fluid, then the tangent of the mean inertial particle trajectory is approximately $\overline{\boldsymbol{V}}_p/|\overline{\boldsymbol{U}}_0|$, where $\overline{\boldsymbol{U}}_0$ is a constant, representative of the mean fluid particle velocity, $\overline{\boldsymbol{U}}$, during a certain interval. Then, we can define

$$\alpha(t)e_z = |\overline{\boldsymbol{U}}_0|^{-2}\left(\overline{\boldsymbol{V}}_p(t) \times \overline{\boldsymbol{U}}(t)\right). \tag{17}$$

By the definition (A32) of temporal mean, it is easy to verify that these mean velocities, $\overline{\boldsymbol{V}}_p$ and $\overline{\boldsymbol{U}}$, represent Poincaré maps of inertial and fluid particle position, respectively, from one period to the next, e.g., $\boldsymbol{X}_p(t+T) = \boldsymbol{X}_p(t) + T\overline{\boldsymbol{V}}_p(t)$. Since all particles undergo clockwise orbits in the streaming cell in the first quadrant, then $\alpha > 0$ implies a tendency of the inertial particle to spiral inward, $\alpha < 0$ a tendency to spiral outward, and $\alpha = 0$ a tendency to stay on the mean Lagrangian streamline. Thus, the particle's motion at a given instant can be explained by examining this quantity, as Figure 5 illustrates. It is instructive to consider this expression at some instant t_0 such that the inertial and fluid particles have been constrained to follow the same trajectory for $t \leq t_0$, so $\alpha(t_0) = 0$, and $\mathrm{d}\alpha/\mathrm{d}t$ expresses the tendency for these trajectories to deviate in the next instant.

First, it is straightforward to show that the temporal mean and derivative operations commute with one another. Thus, at t_0, we can write

$$\frac{\mathrm{d}\alpha}{\mathrm{d}t}e_z = |\overline{\boldsymbol{U}}_0|^{-2}\left(\overline{\frac{\mathrm{d}\boldsymbol{V}_p}{\mathrm{d}t}} \times \overline{\boldsymbol{U}} + \overline{\boldsymbol{V}}_p \times \overline{\frac{\mathrm{d}\boldsymbol{U}}{\mathrm{d}t}}\right). \tag{18}$$

Using a Taylor expansion about a reference position similar to that used in the Appendix for the mean fluid particle velocity, it can be shown that the mean of the relative velocity is

$$\overline{\boldsymbol{w}}(t) = \overline{\boldsymbol{V}}_p(t) - \overline{\boldsymbol{U}}(t) - \boldsymbol{w}_{sd}, \tag{19}$$

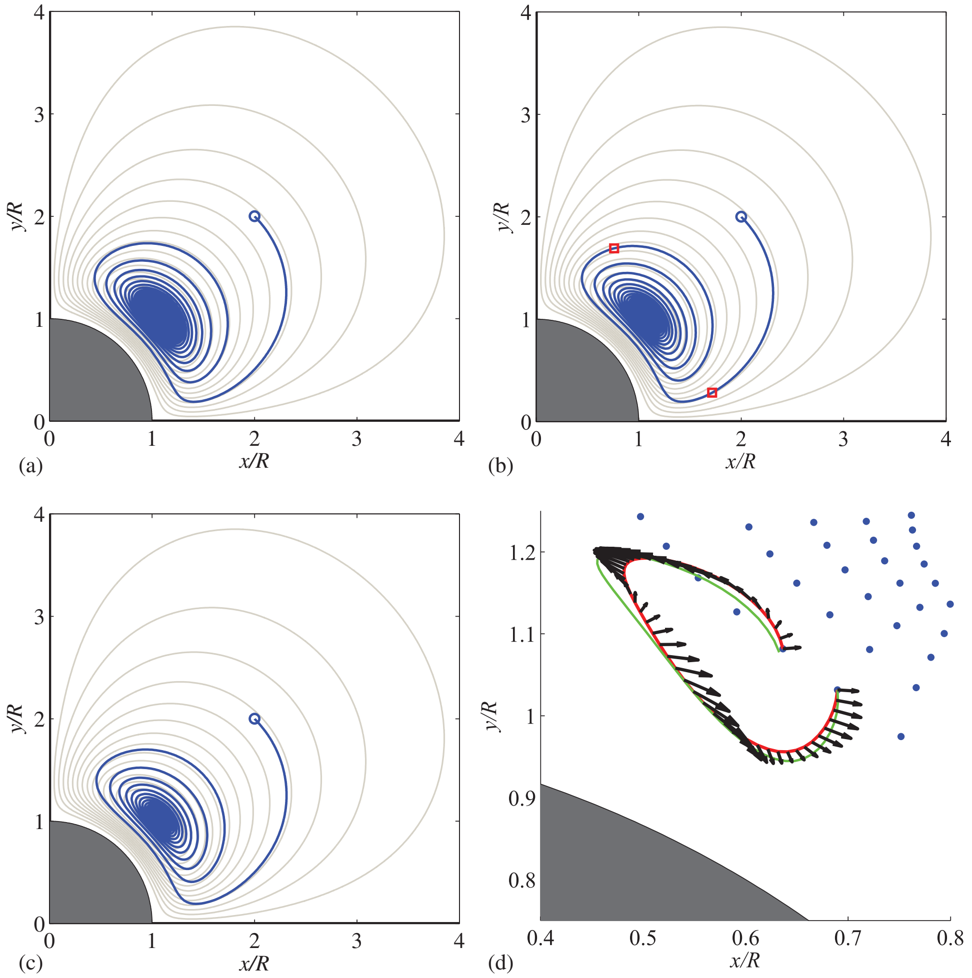

FIG. 3. Panels (a)–(c) Inertial particles trajectories (in dark gray, or blue), sampled once per cycle, for $Re = 40$, $a/R = 0.175$. Initial locations depicted with circles. Lagrangian streamlines are depicted in light gray. (a) $\rho_p/\rho_f = 1.05$, (b) 1, (c) 0.95. In (b), square symbols denote the instants $t/T = 290$ and 350. (d) Inertial (dark gray, or red) and fluid (light gray, or green) particle trajectories over one oscillation cycle, $t/T \in [317, 318]$ for $\rho_p/\rho_f = 1$. Arrows depict the total hydrodynamic force vectors in Eq. (14). Dots denote inertial particle trajectory sampled once per cycle.

where the final term, $\boldsymbol{w}_{sd} = \overline{\int^t \boldsymbol{w}\,\mathrm{d}\tau \cdot \nabla \boldsymbol{u}}$, represents the difference in Stokes drift between the inertial and fluid particles. This term is smaller than the Stokes drift itself, and is therefore not expected to serve a role in determining the inward or outward motion of the inertial particle, so we neglect it in this discussion. Thus, we can equally well define $\mathrm{d}\alpha/\mathrm{d}t$ at t_0 as

$$\frac{\mathrm{d}\alpha}{\mathrm{d}t} e_z = |\overline{\boldsymbol{U}}_0|^{-2} \left(\overline{\frac{\mathrm{d}\boldsymbol{w}}{\mathrm{d}t}} \times \overline{\boldsymbol{U}} + \overline{\boldsymbol{w}} \times \overline{\frac{\mathrm{d}\boldsymbol{U}}{\mathrm{d}t}} \right). \tag{20}$$

In the first term, we can replace $\mathrm{d}\boldsymbol{w}/\mathrm{d}t$ with the MR equation (14), and we note that the temporal mean also commutes with the convolution operator in the Basset term. Thus, we end up with

$$\frac{\mathrm{d}\alpha}{\mathrm{d}t} e_z = |\overline{\boldsymbol{U}}_0|^{-2} \Bigg[C_u \overline{\frac{\mathrm{d}\boldsymbol{U}}{\mathrm{d}t}} \times \overline{\boldsymbol{U}} - C_s \overline{\boldsymbol{w}} \times \overline{\boldsymbol{U}} - C_c \overline{\boldsymbol{w} \cdot \nabla \boldsymbol{U}} \times \overline{\boldsymbol{U}}$$
$$- C_b \int_{-\infty}^{t} \frac{\mathrm{d}/\mathrm{d}\tau \left[\overline{\boldsymbol{w}} - \frac{1}{6}(a/R)^2 \nabla^2 \overline{\boldsymbol{U}}(\boldsymbol{X}_p(\tau), \tau) \right]}{\sqrt{t - \tau}} \mathrm{d}\tau \times \overline{\boldsymbol{U}}$$

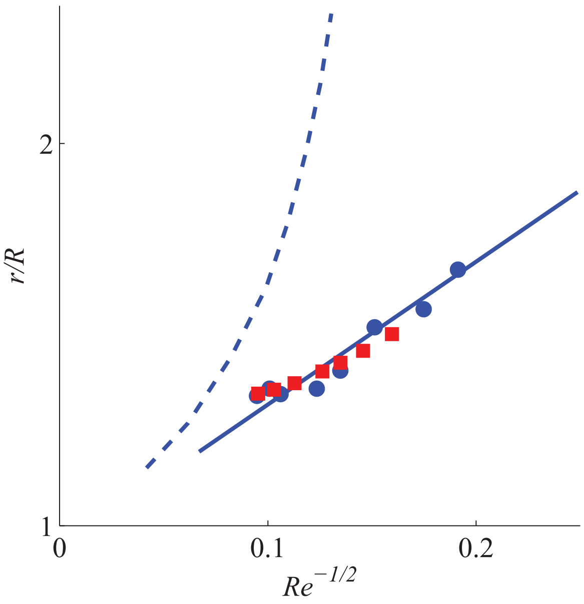

FIG. 4. Comparison of trapping position from current results (squares) and experiments (circles) of Lutz, Chen, and Schwartz.[11] Dashed and solid lines depict, respectively, inner streaming cell size δ_{DC}/R and inner streaming cell center location.

$$+C_l \operatorname{sgn}(G)\overline{|G|^{1/2}|\boldsymbol{w}|\boldsymbol{n}} \times \overline{\boldsymbol{U}}$$

$$\left(C_{f1}\nabla^2\overline{\boldsymbol{U}} + C_{f2}\frac{\mathrm{d}}{\mathrm{d}t}\nabla^2\overline{\boldsymbol{U}}\right) \times \overline{\boldsymbol{U}} + \overline{\boldsymbol{w}} \times \frac{\mathrm{d}\overline{\boldsymbol{U}}}{\mathrm{d}t}\Bigg], \tag{21}$$

where

$$C_u = \frac{1-\rho_p/\rho_f}{\rho_p/\rho_f + 1/2}, \quad C_s = \frac{(9/2)Re_a^{-1}}{\rho_p/\rho_f + 1/2}, \quad C_c = \frac{3/2}{\rho_p/\rho_f + 1/2},$$
$$C_b = \frac{(9/2)\pi^{-1/2}Re_a^{-1/2}}{\rho_p/\rho_f + 1/2}, \quad C_l = \frac{3K Re_a^{-1/2}}{\rho_p/\rho_f + 1/2}, \tag{22}$$
$$C_{f1} = \frac{(3/4)Re_a^{-1}(a/R)^2}{\rho_p/\rho_f + 1/2}, \quad C_{f2} = \frac{(1/20)(a/R)^2}{\rho_p/\rho_f + 1/2}.$$

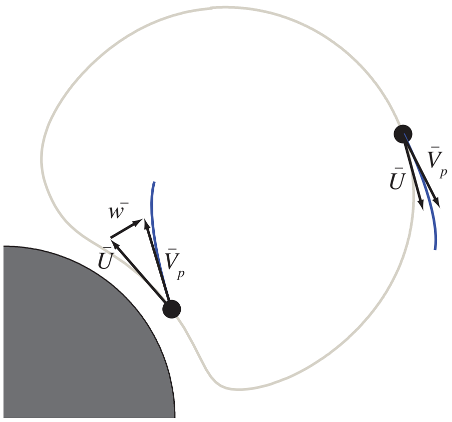

FIG. 5. Illustration of the tendency of a inertial particle to deviate from a Lagrangian streamline. Note that $\alpha < 0$ in the upper right portion of the streamline, and $\alpha > 0$ in the lower left portion.

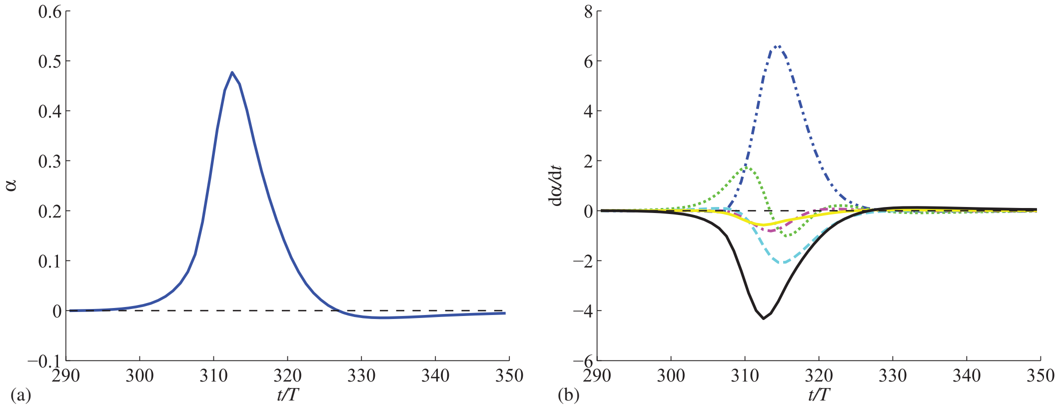

FIG. 6. (a) History of α during the cycle $t/T \in [290, 350]$ for $Re = 40$, $a/R = 0.175$, $\rho_p/\rho_f = 1$. (b) Contributions to $\mathrm{d}\alpha/\mathrm{d}t$ from each term in Eq. (21): Stokes drag (solid black); convective term (dashed, cyan); Basset history (dashed-dotted, magenta); Saffman lift (dashed-dotted-dotted, blue); Faxén corrections (dotted, green); $\overline{\boldsymbol{w}} \times \mathrm{d}\overline{\boldsymbol{U}}/\mathrm{d}t$ (solid light gray, or yellow).

Here, we examine the quantities α and $\mathrm{d}\alpha/\mathrm{d}t$ during the interval between $t/T = 290$ and 350 (between two red squares in Figure 3(b)), when the inertial particle experiences the greatest tendency toward the center of the streaming cell. As Figure 6(a) shows, the value of α remains essentially zero, except for a short interval during which the particle is nearest to the cylinder. During this short interval, α has a positive peak between $t/T = 310$ and 320, followed by a slightly negative value. This behavior is evident in the particle trajectory in Figure 3(b). At the start of the interval, indicated by the first red square, the inertial particle essentially follows the fluid particle trajectory until it reaches the region in which the streamlines of the cell change curvature, from convex (bowed outward) to concave (bowed inward). Here, the inertial particle moves significantly toward the center of the streaming cell, consistent with the positive peak in α. When the particle has traversed this region of concave streamlines, it undergoes a slight outward motion, associated with a slightly negative value of α. Therefore, the inertial particle experiences the most inward motion toward the center of the streaming cell in the portion of trajectory nearest to the cylinder, while it stays on the fluid streamline on the portion farthest from the cylinder. This is evident in Figure 7, which depicts the mean inertial particle trajectory superposed on the mean fluid trajectories, along with the total force

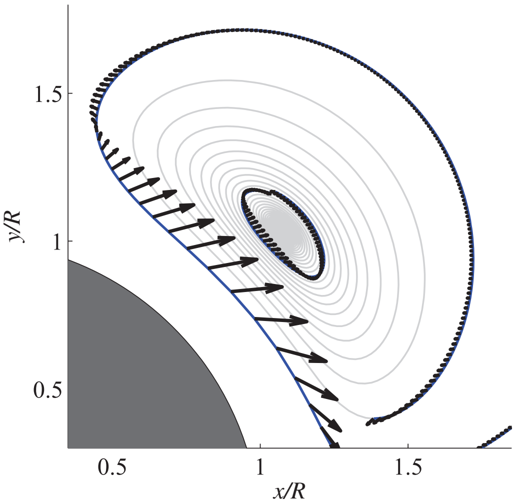

FIG. 7. Hydrodynamic force (arrows) at sampled times along the inertial particle trajectory (dark solid line) during the intervals $t/T \in [0, 485]$ and $t/T \in [1300, 1370]$ for $Re = 40$, $a/R = 0.175$ and $\rho_p/\rho_f = 1$. All portions of the inertial particle trajectory not in these intervals are shown as a light gray line.

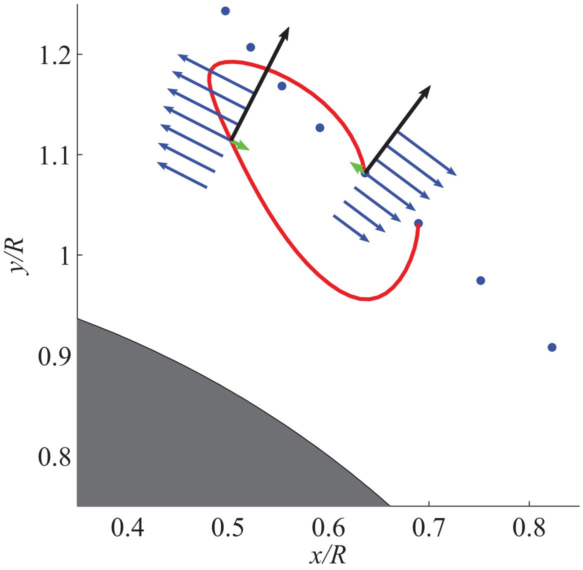

FIG. 8. Saffman lift force (black arrow), relative particle velocity, $\boldsymbol{w}$ (light gray arrow, or green), and local profile of fluid velocity, $\boldsymbol{u}$, perpendicular to $\boldsymbol{w}$ (gray arrows, or blue) at $t/T = 317.5$ and $t/T = 318$. Velocity vectors are plotted with the same scale. Solid line (red) denotes the inertial particle trajectory during the oscillation cycle $t/T \in [317, 318]$. Local fluid particle trajectory, sampled once per period, shown with dots.

on the particle (that is, the right-hand side of Eq. (14) sampled at various instants). This force is largest, and consistently directed toward the center of the streaming cell, when the particle is nearest the cylinder, but its magnitude decreases dramatically when the particle is furthest from the cylinder. With each successive orbit, this process is repeated, until finally the particle becomes trapped at the center of the streaming cell.

Each contribution to $\mathrm{d}\alpha/\mathrm{d}t$ from Eq. (21) is depicted in Figure 6(b). The Faxén terms are the earliest to contribute to positive α, and are countered by the Stokes drag, the convective term, and the Basset history term, which all tend to resist this deviation from the fluid particle trajectory. The Saffman lift initiates its role somewhat later, but ultimately contributes the most positive $\mathrm{d}\alpha/\mathrm{d}t$, and is therefore most responsible for the motion toward the center of the cell. Note that all terms are significant, and none – including the Basset term – can be reliably ignored in the analysis.

The Saffman lift clearly plays an important role in the trapping of inertial particles, so we examine it further. Figure 8 graphically depicts the instantaneous relationships between local fluid velocity gradient, relative velocity $\boldsymbol{w}$, and lift component. Two different instants within a single oscillation cycle are shown. Generically, the Saffman lift is oriented in the gradient direction of increasing velocity when the relative velocity is opposite that of the fluid velocity (i.e., when the particle moves slower than the fluid). This is confirmed in each of the instants shown in Figure 8. Indeed, the component maintains the same direction at both instants shown, since the components of both $\boldsymbol{w}$ and shear rate change sign during the cycle. This ensures that there is a significant mean in the Saffman lift.

It is also important to note that the Saffman lift is only operative when the relative particle velocity, $\boldsymbol{w}$, is non-zero. By (14), there are only two possible mechanisms by which $\boldsymbol{w}$ can become non-zero when it starts at zero: the fluid acceleration term and the Faxén corrections. For a neutrally buoyant particle, the unsteady term vanishes, and thus only the Faxén correction can cause an inertial particle to initially deviate from its fluid trajectory. This is clearly the case here, as indicated by the breakdown of contributions in Figure 6(b): the Faxén term is the earliest to divert the particle from the trajectory of the fluid, as the particle enters the region of significant vorticity gradient. However, once the particle has deviated, the role of the Faxén terms is secondary to that of the Saffman lift.

The final trapping point of the inertial particle is at the center of the Lagrangian streaming cell, and is not dependent on the initial location. Indeed, inertial particles travel toward nearly the

TABLE I. Time averaged forces applied on the inertial particle during the interval $t/T \in [4200, 4700]$ for $Re = 40$, $a/R = 0.175$, $\rho_p/\rho_f = 1$.

	Lift	Faxén	Basset	Convective	Stokes	Total
$F_x/\rho_f R^4 \Omega^2$	5.65×10^{-3}	-3.00×10^{-4}	3.43×10^{-5}	-3.98×10^{-3}	-1.40×10^{-3}	-4.49×10^{-7}
$F_y/\rho_f R^4 \Omega^2$	3.61×10^{-3}	1.12×10^{-2}	-2.41×10^{-4}	2.59×10^{-4}	-1.48×10^{-2}	1.08×10^{-6}

same point, regardless of their size, density, and initial position. We can understand this better by inspecting the mean version of the MR equation (14). The mean fluid particle velocity, $\overline{\boldsymbol{U}}$, vanishes at the center of this cell, and so too does $\mathrm{d}\overline{\boldsymbol{U}}/\mathrm{d}t$ once an inertial particle reaches this center. However, $\nabla\overline{\boldsymbol{U}}$ and $\nabla^2\overline{\boldsymbol{U}}$ do not vanish, and thus several of the forces remain active at the center of the streaming cell, due to continuous motion from the oscillating cylinder. As Table I shows, all forces are small in magnitude in this region, and the Saffman lift and Faxén corrections remain in balance with the Stokes drag and convective term. Thus, the cell center is a fixed point of these mean equations. The continuous trajectory actually converges to a limit cycle, traversed once per oscillation cycle. This is evident in Figure 9, which depicts the limit cycle for neutrally buoyant inertial particles of various size (or particle Reynolds number) and fixed Re. The limit cycle is approximately the same size for all particles, and is nearly concentric with the streaming cell. The orbits have a nearly elliptical shape with a major axis of length $0.25R$ and minor axis of length $0.05R$ (which are likely controlled by ϵ) and are oriented nearly vertically.

A. Inertial particle trapping speed

It was revealed above that a inertial particle spirals inward due to the hydrodynamic forces (primarily the Saffman lift), and eventually gets trapped near the center of the Lagrangian streaming cell in a continuous limit cycle. In the trajectory sampled once per period, this particle converges to a fixed point, and the speed with which it converges is of interest.

The complex mix of forces during the trapping is dependent upon all of the parameters of the problem. Furthermore, the velocity of the particle during this trajectory is similar to that of the

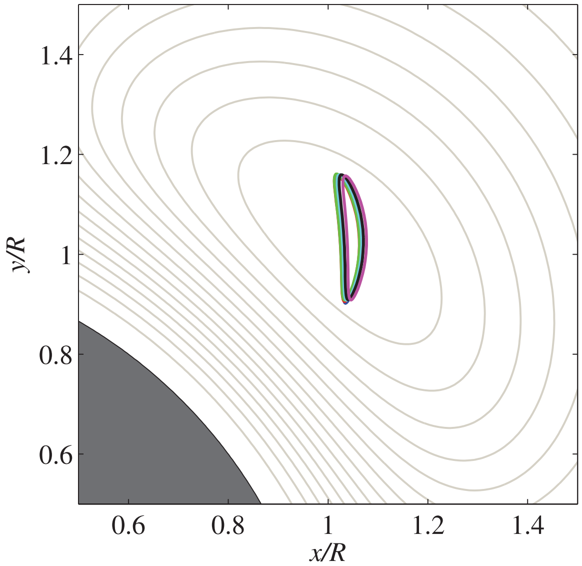

FIG. 9. The final limit cycle for inertial particles of various sizes: $a/R = 0.1$ (blue); $a/R = 0.115$ (red); $a/R = 0.13$ (green); $a/R = 0.145$ (cyan); $a/R = 0.16$ (black); $a/R = 0.175$ (magenta), each plotted over one cycle for $Re = 40$, $\rho_p/\rho_f = 1$. Mean Lagrangian streamlines shown in light gray for reference.

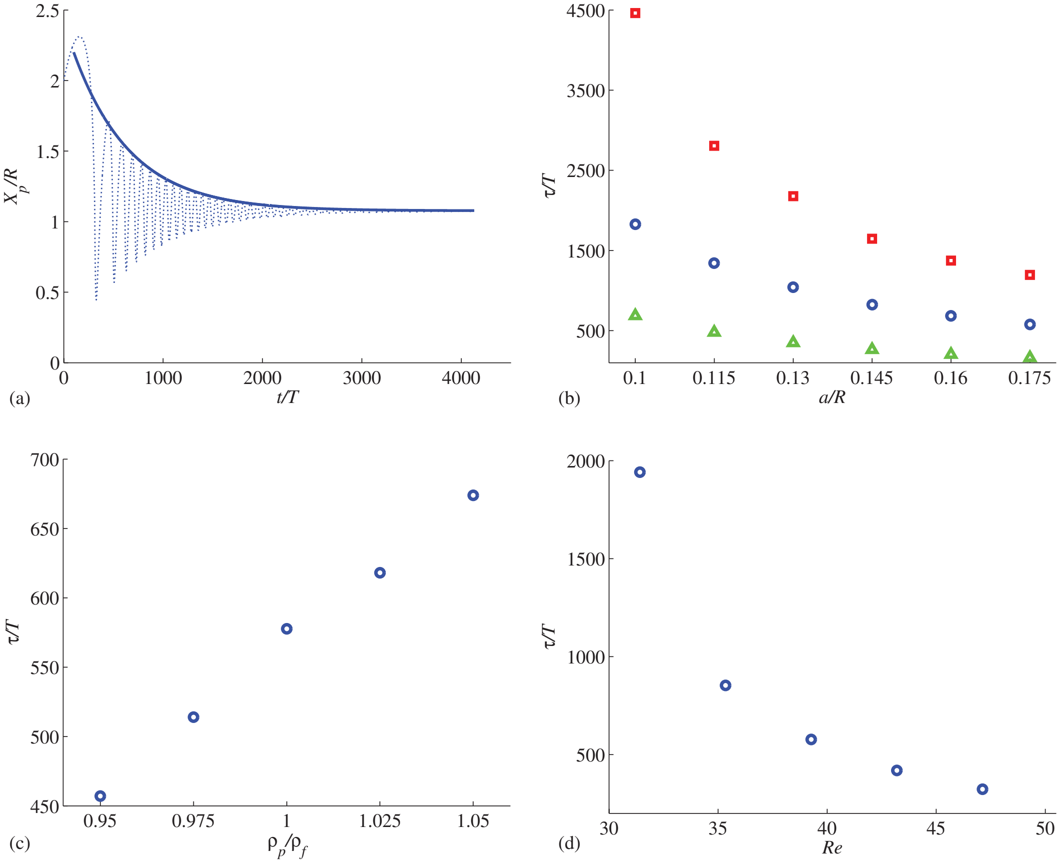

FIG. 10. (a) The sampled history of the x position of an inertial particle (- - -) and an exponential fit to the envelope (—), for $Re = 40$, $\rho_p/\rho_f = 1$, and $a/R = 0.175$. (b) Trapping timescale dependence on a/R, for $Re = 40$, $\rho_p/\rho_f = 1$. This figure contains results for $\epsilon = 0.2\sqrt{2}$ (green triangles), 0.2 (blue circles), 0.1 (red squares). (c) Trapping timescale dependence on ρ_p/ρ_f for $Re = 40$, $a/R = 0.175$. (d) Trapping timescale dependence on Re for $\rho_p/\rho_f = 1$, with a/R varied so that $\Omega a^2/\nu$ is fixed at 1.2.

fluid particle, $V_s \sim \epsilon\Omega A = \epsilon^2\Omega R$. However, the forces on the particle during trapping, notably the Stokes drag and Saffman lift, have a mix of linear and non-linear dependence on velocity. Thus, one expects that τ/T – the timescale of trapping, scaled by period $T = 2\pi/\Omega$ – depends inversely on ϵ to some power, but all parameters – ϵ, Re, a/R, and ρ_p/ρ_f – determine the shape of the spiral trajectory. Thus, the trapping timescale obeys

$$\frac{\tau}{T} = f(\epsilon, Re, a/R, \rho_p/\rho_f). \tag{23}$$

The dashed line in Figure 10(a) is the history of the x component of position of the inertial particle (sampled once per period) and exhibits an asymptotic decay toward a steady position. A criterion to establish convergence is that the difference between two consecutive peaks in this sampled history falls below a threshold value (10^{-4}). Once the inertial particle is determined to be converged, the trapping timescale can be determined by fitting an exponential curve $K\exp(-t/\tau)$ to the envelope of the history, as depicted by the solid line in Figure 10(a).

Three cases are investigated by varying one of the parameters (density, particle size and Reynolds number), while fixing the remaining parameters. Figure 10(b) indicates that, as the size of the particle (and thus, the particle Reynolds number, $Re_a = \Omega a^2/\nu$) increases, so too does the speed of convergence toward the trapping point. This is due to the decreased resistance from the Stokes drag in the MR equation. This term is proportional to the inverse of the particle Reynolds number, whereas the Saffman lift is proportional to the inverse root, and is thus less affected by the increase. This result is consistent with the experimental results of Lutz *et al.*,[38] who found that very small particles are not trapped effectively. Note that Figure 10(b) also exhibits the dependence on ϵ. As expected, the trapping speed is higher as ϵ increases.

Figure 10(c) shows that, as particle density increases, the convergence speed decreases. Inspection of (21) shows that all terms contributing to $\mathrm{d}\alpha/\mathrm{d}t$, except for the unsteady term (with factor C_u), are weakened by an increase in particle inertia. Though this unsteady term can enhance trapping as density ratio increases (by virtue of centripetal acceleration), its effect for density ratios near unity is more than compensated for by the decreased effectiveness of the Saffman lift and Faxén correction terms, which are dominant in this regime.

Finally, Figure 10(d) shows that trapping speed also increases with increasing Reynolds number when the particle Reynolds number is fixed. Since the particle Reynolds number is fixed, the viscous resistance does not change. However, the underlying flow field has been altered by an increase in Re, and particularly, the strengths of the vorticity and velocity gradients have increased. Thus, the Faxén terms and the Saffman lift are enhanced by the stronger gradients, increasing the tendency toward trapping.

B. Inner and outer streaming

The results thus far have focused on the behavior of inertial particles in the inner streaming cell. At Reynolds number $Re = 40$, this cell has a thickness $\delta_{DC} \approx 4.6R$, so that the boundary of the cell is on the periphery of the viewing window in Figure 3. However, this thickness shrinks to $0.82R$ at $Re = 80$, so that the cell is more compact, as shown in Figure 11. It is natural, then, to explore the behavior of inertial particles released from points outside the boundary of the streaming cell. This region is characterized by mean Lagrangian streamlines that do not form closed loops, but rather, direct fluid particles toward the cylinder in the 90° sectors centered on the y axis, and away from the cylinder in the sectors centered on the x axis. Figure 11 depicts the trajectories of a neutrally buoyant inertial particle of radius $a/R = 0.175$ released various points. The particle released from a point well inside the inner streaming cell remains inside the cell and spirals toward a fixed point. Particles released well outside the cell remain outside, and travel approximately along fluid particle trajectories (expected due to the small velocity and vorticity gradients in this region).

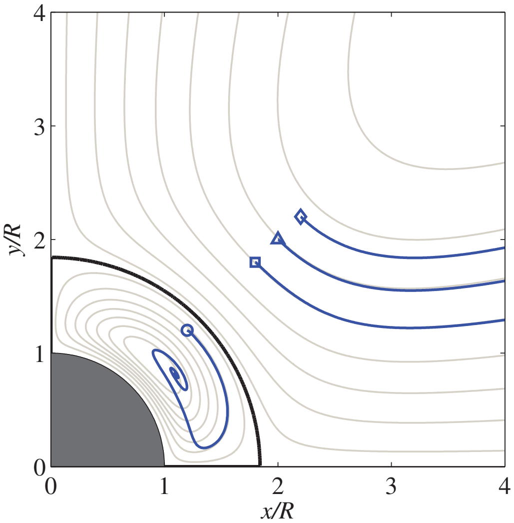

FIG. 11. Inertial particle trajectories at $Re = 80$ for particle of density $\rho_p/\rho_f = 1$ and radius $a/R = 0.175$, initially located at $(1.2R, 1.2R)$ (circle), $(1.8R, 1.8R)$ (square), $(2R, 2R)$ (triangle), $(2.2R, 2.2R)$ (diamond). Lagrangian streamlines are in light gray.

IV. CONCLUSIONS

The behavior of inertial particles in a streaming flow generated by an oscillating circular cylinder has been examined by integrating the Maxey–Riley equation with Saffman lift force in an analytically obtained flow field. The flowfield consists of a primary oscillatory and secondary streaming components, the latter of which consists of a set of four streaming cells surrounding the cylinder. Inertial particles released in the inner streaming cell of this flow exhibit an inward spiral toward a trapping point at the center of streaming cell. The most prominent force responsible for trapping is the Saffman lift force – which itself is activated by the Faxén corrections that divert the particle from the fluid particle trajectory – while viscous forces such as Stokes drag and the Basset history term resist this trapping.

The trapping speed for inertial particles has also been investigated. It has been found that lighter, larger particles are trapped faster, as are particles of a fixed density and particle Reynolds number at larger flow Reynolds number; very small particles, in contrast, exhibit slow trapping speeds and are not effectively trapped. These results have also shown that the particle is trapped at approximately the same location – the center of the streaming cell – regardless of its size, density, or initial location inside the cell. Particles initially outside the streaming cell, however, are repelled rather than trapped. The predicted trapping locations agree well with previous experiments.

In our ongoing work on this topic, we are investigating the feasibility of transporting particles between multiple oscillating cylinders by individually controlling their oscillation parameters – that is, by modulating, or simply creating and destroying, the trapping locations. This will be the subject of a future paper.

ACKNOWLEDGMENTS

Support for this work by the National Science Foundation, under Award Nos. CMMI-0969869 and CMMI-1000656, is gratefully acknowledged. The authors would also like to thank Dr. Phanindra Tallapragada, for many helpful discussions.

APPENDIX: FLOW GENERATED BY CIRCULAR CYLINDER IN OSCILLATORY FREE STREAM

The derivation summarized here follows that of Holtsmark *et al.*[21] with some minor modifications made to the notation, and corrects some errors in the second-order oscillatory portion of their solution. Additional consideration is given to the Lagrangian streamfunction and associated Stokes drift, and this is adapted from the work of Longuet-Higgins[39] and Raney, Corelli, and Westervelt.[22]

The cylinder is at rest and the fluid at infinity is in uniform oscillatory motion in the x direction, with velocity $U(t) = -A\Omega\cos(\Omega t)$. We seek the solution of the two-dimensional vorticity transport equation,

$$\frac{\partial}{\partial t}(\nabla^2\psi) + \boldsymbol{u}\cdot\nabla(\nabla^2\psi) = \nu\nabla^4\psi \tag{A1}$$

subject to the conditions

$$\psi = 0,\ \frac{\partial\psi}{\partial r} = 0 \text{ at } r = R, \qquad \psi \to -A\Omega r\sin\theta\cos\Omega t \text{ as } r\to\infty, \tag{A2}$$

where the polar velocity components are defined as

$$u_r = \frac{1}{r}\frac{\partial\psi}{\partial\theta}, \quad u_\theta = -\frac{\partial\psi}{\partial r}. \tag{A3}$$

From hereon, the variables are scaled by R and Ω. We thereby arrive at the dimensionless form of the problem

$$\nabla^2\left(\nabla^2 - Re\frac{\partial}{\partial t}\right)\psi = Re\,\boldsymbol{u}\cdot\nabla\left(\nabla^2\psi\right) \tag{A4}$$

and

$$\psi = 0,\ \frac{\partial \psi}{\partial r} = 0 \text{ at } r = 1, \qquad \psi \to -\epsilon r \sin\theta \cos t \text{ as } r \to \infty. \tag{A5}$$

We introduce an asymptotic expansion in ϵ for the streamfunction,

$$\psi = \epsilon\psi_1 + \epsilon^2\psi_2 + O(\epsilon^3) \tag{A6}$$

and thereby develop a hierarchy of problems for ψ_1, ψ_2, etc. We will restrict our attention here to the first two,

$$\nabla^2\left(\nabla^2 - Re\frac{\partial}{\partial t}\right)\psi_1 = 0, \tag{A7}$$

$$\psi_1 = 0,\ \frac{\partial \psi_1}{\partial r} = 0 \quad \text{at } r = 1, \qquad \psi_1 \to -r \sin\theta \cos t \text{ as } r \to \infty$$

and

$$\nabla^2\left(\nabla^2 - Re\frac{\partial}{\partial t}\right)\psi_2 = Re\,\boldsymbol{u}_1 \cdot \nabla\left(\nabla^2\psi_1\right), \tag{A8}$$

$$\psi_2 = 0,\ \frac{\partial \psi_2}{\partial r} = 0 \text{ at } r = 1, \qquad \psi_2 \to 0 \text{ as } r \to \infty.$$

1. First-order solution

Equation (A7) for the first-order streamfunction is linear and homogeneous, and consists of a superposition of solutions of the two-dimensional Laplace equation and heat equation. This first-order solution comprises the forcing – via Reynolds stresses – for the second-order equation (A8). It is interesting to note that, if the oscillatory motion of the cylinder were changed in sign (i.e., phase-shifted by π), the second-order motion would be unaffected.

The solution of (A7) can be written as

$$\psi_1(r,\theta,t) = \mathrm{Re}\left(\Psi_1(r)\mathrm{e}^{-\mathrm{i}t}\right)\sin\theta, \tag{A9}$$

where the radial dependence can be split into two parts

$$\Psi_1(r) = \Psi_1^{(1)}(r) + \Psi_1^{(2)}(r), \tag{A10}$$

each of which represents the homogeneous solution of one of the two differential operators in (A7); $\Psi_1^{(1)}$ is the radial dependence of the solution of the Laplace equation and $\Psi_1^{(2)}$ of the heat equation. After applying boundary conditions, these solutions are, respectively,

$$\Psi_1^{(1)}(r) = \ -r - \frac{C}{r}, \tag{A11}$$

$$\Psi_1^{(2)}(r) = \frac{2H_1^{(1)}(\gamma r)}{\gamma H_0^{(1)}(\gamma)} = r\left[\frac{H_0^{(1)}(\gamma r)}{H_0^{(1)}(\gamma)} + \frac{H_2^{(1)}(\gamma r)}{H_0^{(1)}(\gamma)}\right], \tag{A12}$$

where $C = H_2^{(1)}(\gamma)/H_0^{(1)}(\gamma)$. Note that $H_1^{(1)}$ and $H_1^{(2)}$ are the first-order Hankel functions of the first and second kind, respectively, and $\gamma = (\mathrm{i}Re)^{1/2}$. When streamfunction is expressed in the inertial reference frame (in which the cylinder is in motion and the fluid at rest at infinity), the first term in (A11) is cancelled by the first-order modification in the change of reference frame equation (7).

The velocity components associated with this first-order streamfunction are

$$u_{r,1} = \mathrm{Re}\left(U_{r,1}(r)\mathrm{e}^{-\mathrm{i}t}\right)\cos\theta \tag{A13}$$

and

$$u_{\theta,1} = \mathrm{Re}\left(U_{\theta,1}(r)\mathrm{e}^{-\mathrm{i}t}\right)\sin\theta, \tag{A14}$$

where $U_{r,1} = \Psi_1/r$ and $U_{\theta,1} = -\mathrm{d}\Psi_1/\mathrm{d}r$. It is straightforward to show (using recurrence relations for Hankel functions) that

$$U_{r,1}(r) = -1 - \frac{C}{r^2} + \frac{H_0^{(1)}(\gamma r)}{H_0^{(1)}(\gamma)} + \frac{H_2^{(1)}(\gamma r)}{H_0^{(1)}(\gamma)}, \tag{A15}$$

$$U_{\theta,1}(r) = 1 - \frac{C}{r^2} - \frac{H_0^{(1)}(\gamma r)}{H_0^{(1)}(\gamma)} + \frac{H_2^{(1)}(\gamma r)}{H_0^{(1)}(\gamma)}. \tag{A16}$$

2. Second-order solution

The first-order solution can now be used to evaluate the forcing term in Eq. (A8) for ψ_2. It can be verified that this leads to a second-order solution of the form

$$\psi_2(r,\theta,t) = \mathrm{Re}\left(\Psi_2^s(r) + \Psi_2(r)\mathrm{e}^{-\mathrm{i}2t}\right)\sin 2\theta, \tag{A17}$$

where the radial dependence of the steady solution is

$$\begin{aligned}\Psi_2^s(r) = {}& -\frac{r^4}{48}\int_r^\infty \frac{f_0(\tau)}{\tau}\,\mathrm{d}\tau + \frac{r^2}{16}\int_r^\infty \tau f_0(\tau)\,\mathrm{d}\tau \\ & + \frac{1}{16}\left(\int_1^r \tau^3 f_0(\tau)\,\mathrm{d}\tau + \int_1^\infty \frac{f_0(\tau)}{\tau}\,\mathrm{d}\tau - 2\int_1^\infty \tau f_0(\tau)\,\mathrm{d}\tau\right) \\ & + \frac{1}{r^2}\left(-\frac{1}{48}\int_1^r \tau^5 f_0(\tau)\,\mathrm{d}\tau - \frac{1}{24}\int_1^\infty \frac{f_0(\tau)}{\tau}\,\mathrm{d}\tau + \frac{1}{16}\int_1^\infty \tau f_0(\tau)\,\mathrm{d}\tau\right),\end{aligned} \tag{A18}$$

where

$$f_0(r) = \frac{\mathrm{i}Re^2}{4}\frac{1}{r}\left(\Psi_1\frac{\mathrm{d}\Psi_1^{(2)*}}{\mathrm{d}r} - \Psi_1^{(2)*}\frac{\mathrm{d}\Psi_1}{\mathrm{d}r}\right). \tag{A19}$$

The radial dependence of the oscillatory portion is

$$\begin{aligned}\Psi_2(r) = {}& \frac{\mathrm{i}\pi}{4\lambda^2 H_1^{(1)}(\lambda)}\left(H_2^{(1)}(\lambda r)\int_1^r \tau K_2(\lambda\tau)g_0(\tau)\,\mathrm{d}\tau + K_2(\lambda r)\int_r^\infty \tau H_2^{(1)}(\lambda\tau)g_0(\tau)\,\mathrm{d}\tau\right) \\ & + \frac{1}{\lambda^3 H_1^{(1)}(\lambda)}\left[\left(H_2^{(1)}(\lambda r) - r^{-2}H_2^{(1)}(\lambda)\right)\int_1^\infty \frac{g_0(\tau)}{\tau}\,\mathrm{d}\tau + r^{-2}\int_1^\infty \tau H_2^{(1)}(\lambda\tau)g_0(\tau)\,\mathrm{d}\tau\right] \\ & - \frac{1}{4\lambda^2}\left(r^2\int_r^\infty \frac{g_0(\tau)}{\tau}\,\mathrm{d}\tau - r^{-2}\int_1^\infty \frac{g_0(\tau)}{\tau}\,\mathrm{d}\tau + r^{-2}\int_1^r \tau^3 g_0(\tau)\,\mathrm{d}\tau\right),\end{aligned} \tag{A20}$$

where $\lambda = \sqrt{2}\gamma$, $K_2(\lambda\tau) = H_1^{(1)}(\lambda)H_2^{(2)}(\lambda\tau) - H_1^{(2)}(\lambda)H_2^{(1)}(\lambda\tau)$, and

$$g_0(r) = -\frac{\mathrm{i}Re^2}{4r}\left(\Psi_1^{(1)}\frac{\mathrm{d}\Psi_1^{(2)}}{\mathrm{d}r} - \Psi_1^{(2)}\frac{\mathrm{d}\Psi_1^{(1)}}{\mathrm{d}r}\right). \tag{A21}$$

We note that (A20) corrects errors in the solution presented by Holtsmark *et al.*[21]

The velocity components of the second-order solution are, correspondingly,

$$u_{r,2} = \mathrm{Re}\left(\frac{2\Psi_2^s}{r} + \frac{2\Psi_2}{r}\mathrm{e}^{-\mathrm{i}2t}\right)\cos 2\theta \tag{A22}$$

and

$$u_{\theta,2} = -\mathrm{Re}\left(\frac{\mathrm{d}\Psi_2^s}{\mathrm{d}r} + \frac{\mathrm{d}\Psi_2}{\mathrm{d}r}\mathrm{e}^{-\mathrm{i}2t}\right)\sin 2\theta. \tag{A23}$$

The second-order reference frame correction in (7) can be expressed in a complex form similar to the expressions for ψ_1 and ψ_2. We can show, using the decomposition (A9) and rotating the x-derivative to polar coordinates, that the correction is

$$-\sin t\,\frac{\partial\psi_1}{\partial x} = -\mathrm{Re}\left[\frac{\mathrm{i}}{4}\left(\frac{\Psi_1}{r} - \frac{\mathrm{d}\Psi_1}{\mathrm{d}r}\right)\left(1 - \mathrm{e}^{-\mathrm{i}2t}\right)\right]\sin 2\theta. \tag{A24}$$

This correction has the same azimuthal dependence as the second-order streamfunction (A17), and contributes both a mean and an oscillatory part (at twice the forcing frequency). In other words, the corrected form of the second-order streamfunction in the inertial reference frame can be obtained by making the replacements

$$\Psi_2^s \to \Psi_2^s - \frac{\mathrm{i}}{4}\left(U_{r,1} + U_{\theta,1}\right), \qquad \Psi_2 \to \Psi_2 + \frac{\mathrm{i}}{4}\left(U_{r,1} + U_{\theta,1}\right). \tag{A25}$$

The second-order velocity components are correspondingly corrected.

It is interesting to note that this steady portion of the flow has an associated vorticity field that decays algebraically with distance, in contrast to the exponential decay of the oscillatory part of the flow. Though it is difficult to show this with the solution (A18) presented here, the matched asymptotic analysis of Schlichting[19] reveals that the mean vorticity is $\overline{\varpi} \sim 3\epsilon^2 r^{-2}\sin 2\theta$ as $r \to \infty$. This reflects the fact that the dominant steady streaming in the outer region is Stokes flow, and therefore a solution of $\nabla^2\overline{\varpi} = 0$.

3. Fluid particle streaming and the Lagrangian streamfunction

The steady portion of the streamfunction solved for in Subsection A 2 of the Appendix represents the mean Eulerian streamlines of the flow, as depicted in Figure 12(a). Fluid particles do not follow these streamlines in the mean, however. The velocity $\boldsymbol{U}$ of a fluid particle can be expressed in terms of the fluid velocity as

$$\boldsymbol{U}(t) = \boldsymbol{u}\left(\boldsymbol{x}_0 + \int_0^t \boldsymbol{U}\,\mathrm{d}\tau, t\right), \tag{A26}$$

where $\boldsymbol{x}_0$ is the location of the fluid particle at $t = 0$. Over one cycle, the excursion of the fluid particle from $\boldsymbol{x}_0$ is small, and it is therefore possible to expand about this point:

$$\boldsymbol{U}(t) \approx \boldsymbol{u}(\boldsymbol{x}_0, t) + \int_0^t \boldsymbol{U}\,\mathrm{d}\tau \cdot \nabla\boldsymbol{u}(\boldsymbol{x}_0, t). \tag{A27}$$

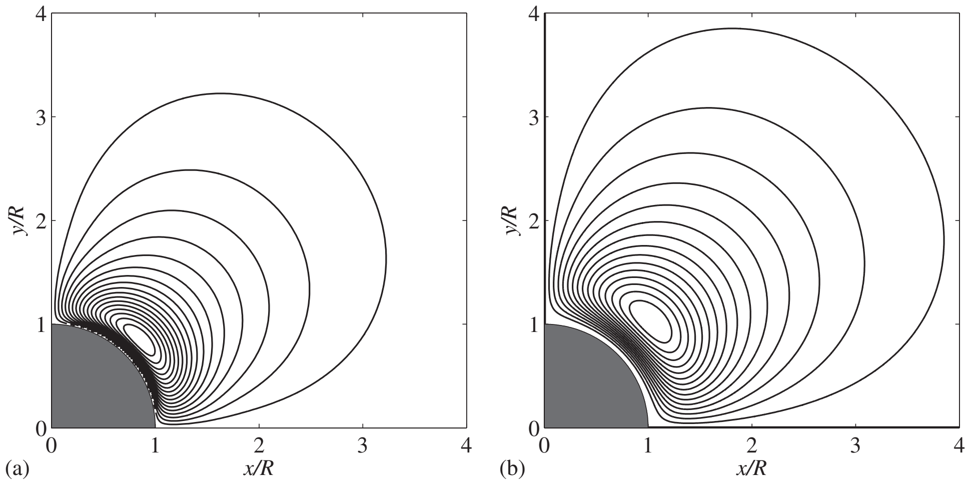

FIG. 12. (a) Mean Eulerian streamlines, and (b) mean Lagrangian streamlines, for $Re = 40$.

Then, we can one again write the asymptotic expansions in ϵ for the fluid velocities,

$$\boldsymbol{u} = \epsilon \boldsymbol{u}_1 + \epsilon^2 \boldsymbol{u}_2, \tag{A28}$$

$$\boldsymbol{U} = \epsilon \boldsymbol{U}_1 + \epsilon^2 \boldsymbol{U}_2, \tag{A29}$$

and substitute them into Eq. (A27) and order in powers of ϵ. As a result, we obtain

$$\boldsymbol{U}_1 = \boldsymbol{u}_1, \tag{A30}$$

$$\boldsymbol{U}_2 = \boldsymbol{u}_2 + \int_0^t \boldsymbol{u}_1 \, \mathrm{d}\tau \cdot \nabla \boldsymbol{u}_1. \tag{A31}$$

We define the temporal mean, $\overline{(\cdot)}$, in this work over one period of oscillation as

$$\overline{f}(t) = \frac{1}{T} \int_t^{t+T} f(\tau) \, \mathrm{d}\tau. \tag{A32}$$

Note that $\boldsymbol{u}_1$, and thus $\boldsymbol{U}_1$, has zero mean. However, the mean of (A31) is

$$\overline{\boldsymbol{U}}_2 = \overline{\boldsymbol{u}}_2 + \overline{\int_0^t \boldsymbol{u}_1 \, \mathrm{d}\tau \cdot \nabla \boldsymbol{u}_1}. \tag{A33}$$

Thus, the mean second-order motion of the fluid particle (that is, the leading-order mean motion) requires a correction: the Stokes drift. One can show, using the incompressibility of $\boldsymbol{u}_1$ and the relation $\overline{g \int^t f \, \mathrm{d}\tau} = -\overline{f \int^t g \, \mathrm{d}\tau}$ for periodic functions f and g, that this correction can be written as

$$\overline{\int_0^t \boldsymbol{u}_1 \, \mathrm{d}\tau \cdot \nabla \boldsymbol{u}_1} = \frac{1}{2} \nabla \times \left(\overline{\boldsymbol{u}_1 \times \int_0^t \boldsymbol{u}_1 \, \mathrm{d}\tau} \right). \tag{A34}$$

Thus, the correction to streamfunction is readily available, and one can define the Lagrangian streamfunction – which defines the mean integral curves of fluid particles – as

$$\psi^L = \psi_2^s + \frac{1}{2} \left(\overline{\boldsymbol{u}_1 \times \int_0^t \boldsymbol{u}_1 \, \mathrm{d}\tau} \right) \cdot e_z. \tag{A35}$$

This streamfunction has the same θ dependence as ψ_2^s. After the reference frame transformation in Sec. II A is made to the first and second order velocities, the radial dependence of the Lagrangian stream function can be expressed as

$$\Psi^L(r) = \Psi_2^s(r) + \frac{1}{2} \mathrm{Im}\left[-\frac{C}{r^2} + \frac{H_2^{(1)}(\gamma r)}{H_0^{(1)}(\gamma)} \right] + \frac{1}{2} \mathrm{Im}\left[\left(\frac{C}{r^2} - \frac{H_2^{(1)}(\gamma r)}{H_0^{(1)}(\gamma)} \right) \left(\frac{H_0^{(1)}(\gamma r)}{H_0^{(1)}(\gamma)} \right)^* \right]. \tag{A36}$$

The third term of Eq. (A36) represents the Stokes drift, the difference between mean Eulerian streamlines and Lagrangian (fluid particle) streaming. The Lagrangian stream function is exhibited in Figure 12(b), which reveals the fluid particle's trajectory.

[1] A. Ashkin, "Acceleration and trapping of particles by radiation pressure," Phys. Rev. Lett. **24**, 156–159 (1970).

[2] J. E. Molloy and M. J. Padgett, "Lights, action: Optical tweezers," Contemp. Phys. **43**, 241–258 (2002).

[3] P. Y. Chiou, A. T. Ohta, and M. C. Wu, "Massively parallel manipulation of single cells and microparticles using optical images," Nature (London) **436**, 370–372 (2005).

[4] H. M. Hertz, "Standing-wave acoustic trap for nonintrusive positioning of microparticles," J. Appl. Phys. **78**, 4845–4849 (1995).

[5] A. Haake, A. Neild, G. Radziwill, and J. Dual, "Positioning, displacement, and localization of cells using ultrasonic forces," Biotechnol. Bioeng. **92**, 8–14 (2005).

[6] M. P. Hughes, "Strategies for dielectrophoretic separation in laboratory-on-a-chip systems," Electrophoresis **23**, 2569–2582 (2002).

[7] J. H. Nieuwenhuis, A. Jachimowicz, P. Svasek, and M. J. Vellekoop, "Optimization of microfluidic particle sorters based on dielectrophoresis," IEEE Sens. J. **5**, 810–816 (2005).

[8] D. Di Carlo, N. Aghdam, and L. P. Lee, “Single-cell enzyme concentrations, kinetics, and inhibition analysis using high-density hydrodynamic cell isolation arrays,” Anal. Chem. **78**, 4925–4930 (2006).

[9] D. Di Carlo, L. Y. Wu, and L. P. Lee, “Dynamic single cell culture array,” Lab Chip **6**, 1445–1449 (2006).

[10] B. R. Lutz, J. Chen, and D. T. Schwartz, “Microscopic steady streaming eddies created around short cylinders in a channel: Flow visualization and Stokes layer scaling,” Phys. Fluids **17**, 023601 (2005).

[11] B. R. Lutz, J. Chen, and D. T. Schwartz, “Hydrodynamic tweezers: 1. Noncontact trapping of single cells using steady streaming microeddies,” Anal. Chem. **78**, 5429–5435 (2006).

[12] V. H. Lieu, T. A. House, and D. T. Schwartz, “Hydrodynamic tweezers: Impact of design geometry on flow and microparticle trapping,” Anal. Chem. **84**, 1963–1968 (2012).

[13] P. Marmottant and S. Hilgenfeldt, “Microacoustics: Controlled vesicle deformation and lysis by single oscillating bubbles,” Nature (London) **423**, 153–156 (2003).

[14] P. Marmottant, J. P. Raven, H. Gardeniers, J. G. Bomer, and S. Hilgenfeldt, “Microfluidics with ultrasound-driven bubbles,” J. Fluid Mech. **568**, 109–118 (2006).

[15] P. Marmottant and S. Hilgenfeldt, “A bubble-driven microfluidic transport element for bioengineering,” Proc. Natl. Acad. Sci. U.S.A. **101**, 9523–9527 (2004).

[16] C. Wang, S. V. Jalikop, and S. Hilgenfeldt, “Size-sensitive sorting of microparticles through control of flow geometry,” Appl. Phys. Lett. **99**, 034101 (2011).

[17] L. Rayleigh, “On the circulation of air observed in Kundt’s tubes, and on some allied acoustical problems,” Philos. Trans. R. Soc. London **175**, 1–21 (1884).

[18] E. N. d. C. Andrade, “On the circulations caused by the vibration of air in a tube,” Proc. R. Soc. London, Ser. A **134**, 445–470 (1931).

[19] H. Schlichting, “Berechnung ebener periodischer Grenzschichtströmungen,” Phys. Z. **33**, 327–335 (1932).

[20] C.-Y. Wang, “On high-frequency oscillatory viscous flows,” J. Fluid Mech. **32**, 55–68 (1968).

[21] J. Holtsmark, I. Johnsen, T. Sikkeland, and S. Skavlem, “Boundary layer flow near a cylindrical obstacle in an oscillating, incompressible fluid,” J. Acoust. Soc. Am. **26**, 26–39 (1954).

[22] W. P. Raney, J. C. Corelli, and P. J. Westervelt, “Acoustical streaming in the vicinity of a cylinder,” J. Acoust. Soc. Am. **26**, 1006–1014 (1954).

[23] A. Bertelsen, A. Svardal, and S. Tjøtta, “Nonlinear streaming effects associated with oscillating cylinders,” J. Fluid Mech. **59**, 493–511 (1973).

[24] N. Riley, “Oscillating viscous flows,” Mathematika **12**, 161–175 (1965).

[25] J. Stuart, “Double boundary layers in oscillatory viscous flow,” J. Fluid Mech. **24**, 673–687 (1966).

[26] A. B. Basset, *A Treatise on Hydrodynamics*, Vol. II (Deighton, Bell, London, 1888).

[27] J. Boussinesq, *Theorie Analytique de la Chaleur*, Vol. II (L’Ecole Polytechnique, Paris, 1903).

[28] C. W. Oseen, *Neuere Methoden und Ergebnisse in der Hydrodynamik* (Akademische Verlagsgesellschaft, Leipzig, 1927).

[29] M. R. Maxey and J. J. Riley, “Equation of motion for a small rigid sphere in a nonuniform flow,” Phys. Fluids **26**, 883–889 (1983).

[30] P. G. Saffman, “The lift on a small sphere in a slow shear flow,” J. Fluid Mech. **22**, 385–400 (1965).

[31] R. L. Panton, *Incompressible Flow*, 2nd ed. (John Wiley and Sons, New York, 1996).

[32] K. K. Tio, A. Liñán, J. C. Lasheras, and A. M. Gañán-Calvo, “On the dynamics of buoyant and heavy particles in a periodic Stuart vortex flow,” J. Fluid Mech. **254**, 671–699 (1993).

[33] A. Daitche and T. Tél, “Memory effects are relevant for chaotic advection of inertial particles,” Phys. Rev. Lett. **107**, 244501 (2011).

[34] F. Candelier, J. R. Angilella, and M. Souhar, “On the effect of the Boussinesq–Basset force on the radial migration of a Stokes particle in a vortex,” Phys. Fluids **16**, 1765–1776 (2004).

[35] F. Candelier, J. R. Angilella, and M. Souhar, “On the effect of inertia and history forces on the slow motion of a spherical solid or gaseous inclusion in a solid-body rotation flow,” J. Fluid Mech. **545**, 113–139 (2005).

[36] N. Mordant and J.-F. Pintona, “Velocity measurement of a settling sphere,” Eur. Phys. J. B **18**, 343–352 (2000).

[37] M. A. T. van Hinsberg, J. H. M. ten Thije Boonkkamp, and H. J. J. Clercx, “An efficient, second order method for the approximation of the Basset history force,” J. Comput. Phys. **230**, 1465–1478 (2011).

[38] B. R. Lutz, personal communication (2012).

[39] M. S. Longuet-Higgins, “Mass transport in water waves,” Philos. Trans. R. Soc. London, Ser. A **245**, 535–581 (1953).